Bioconjugate Chemistry

Article

pubs.acs.org/bc

Synthesis and In Vivo Evaluation of the Biodistribution of a ^{18}F-Labeled Conjugate Gold-Nanoparticle-Peptide with Potential Biomedical Application

Simon Guerrero,[†,□] José Raul Herance,[‡,□] Santiago Rojas,[‡] Juan F. Mena,[†] Juan Domingo Gispert,[‡] Gerardo A. Acosta,[§,∥] Fernando Albericio,*[,§,∥,⊥] and Marcelo J. Kogan*[,†,#]

[†]Departamento de Química Farmacológica y Toxicológica, Facultad de Ciencias Químicas y Farmacéuticas, Universidad de Chile, Sergio Livingstone 1007, Independencia, Santiago, Chile

[‡]Institut d'Alta Tecnologia/CRC Centre d'Imatge Molecular - Parc de Recerca Biomedica de Barcelona, C/Dr, Aiguader 88, 08003, Barcelona, Spain

[§]Institute for Research in Biomedicine, Barcelona Science Park, Baldiri Reixac 10, E-08028, Barcelona, Spain

[∥]CIBER-BBN, Networking Centre on Bioengineering, Biomaterials and Nanomedicine, Barcelona Science Park, Baldiri Reixac 10, E-08028, Barcelona, Spain

[⊥]Department of Organic Chemistry, University of Barcelona, Martí i Franquès 1, 08028, Barcelona, Spain

[#]Centro para la Investigación Interdisciplinaria Avanzada en Ciencias de los Materiales (CIMAT), Santiago, Chile

Ⓢ *Supporting Information*

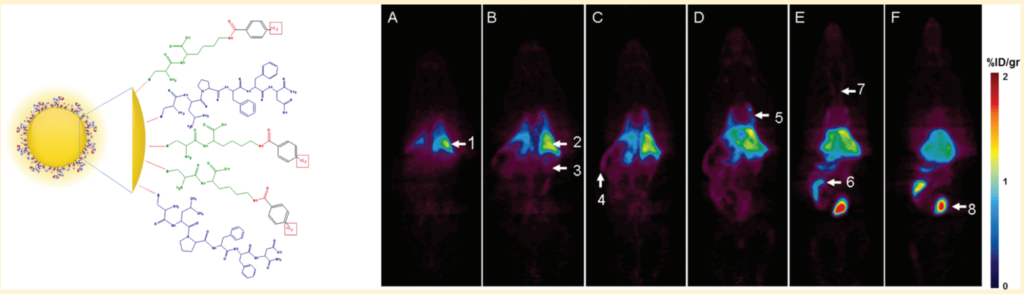

ABSTRACT: Gold nanoparticles (AuNPs) have been extensively used in biological applications because of their biocompatibility, size, and ease of characterization, as well as an extensive knowledge of their surface chemistry. These features make AuNPs readily exploitable for biomedical applications, including drug delivery and novel diagnostic and therapeutic approaches. In a previous work, we studied *ex vivo* distribution of the conjugate C(AuNP)-LPFFD for its potential uses in the treatment of Alzheimer's disease. In this study, we covalently labeled the conjugate with [^{18}F]-fluorobenzoate to study the *in vivo* distribution of the AuNP by positron emission tomography (PET). After intravenous administration in rat, the highest concentration of the radiolabeled conjugate was found in the bladder and urine with a lower proportion in the intestine, demonstrating progressive accumulation compatible with biliary excretion of the conjugate. The conjugate also accumulated in the liver and spleen. PET imaging allowed us to study the *in vivo* biodistribution of the AuNPs in a noninvasive and sensitive way using a reduced number of animals. Our results show that AuNPs can be covalently and radioactively labeled for PET biodistribution studies.

■ INTRODUCTION

Gold nanoparticles (AuNPs) have been extensively used in biological applications because of their biocompatibility, size, and ease of characterization, as well as an extensive knowledge of their surface chemistry. These features make AuNPs readily exploitable for biomedical applications,[1] including drug delivery and novel diagnostic and therapeutic approaches.[2−4] These particles have been used in cancer therapy as molecular surgery tools for the destruction of cancer cells and for the selective killing of bacteria that cause a variety of cutaneous infections.[5]

In a previous study, we demonstrated the ability of targeted spherical AuNPs conjugated to the amphipathic peptide CLPFFD to remove the toxic β-amyloid aggregates involved in Alzheimer's disease and their remote removal by locally applied irradiation with weak microwaves.[6,7] Recently, we showed in a biodistribution study that 12-nm-diameter C(AuNP)LPFFD conjugates increase the penetration of these particles into the rat brain.[8] However, an important drawback is that these experiments were performed *ex vivo* and that they are not fully representative of *ante mortem* conditions. To study the

Received: July 16, 2011
Revised: January 19, 2012
Published: January 30, 2012

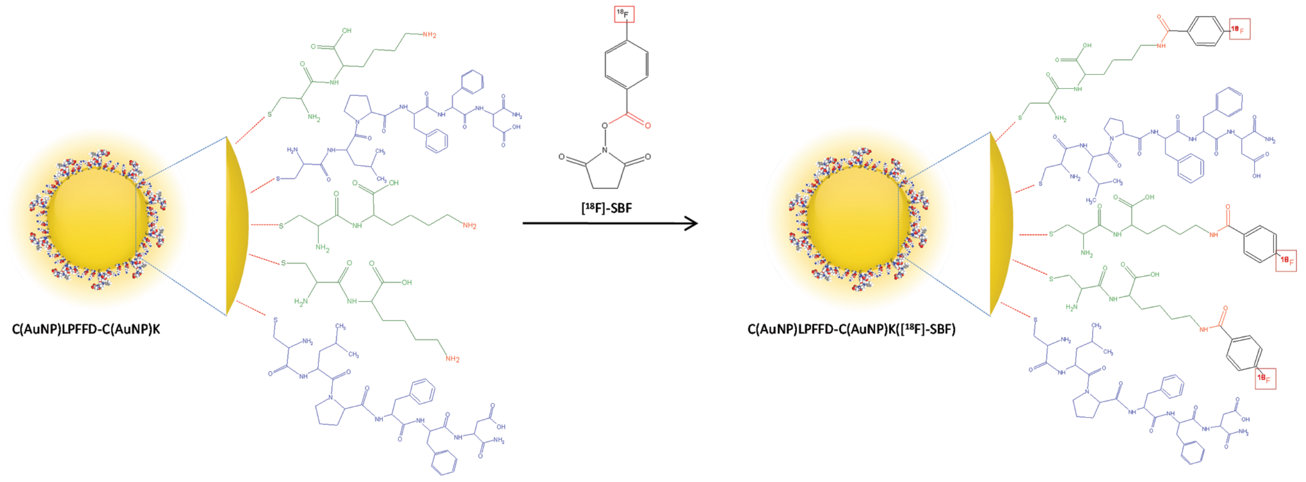

Figure 1. Chemical structures of the peptides attached to the nanoparticle and of the ^{18}F-SFB probe. The CK and CLPFFD peptides are represented in green and blue, respectively. The exposed amino group of the CK peptide and the carbonyl group of the [^{18}F]-SFB probe are shown in red (left). After reaction with the probe, the labeled conjugate C(AuNP)LPFFD-C(AuNP)K([^{18}F]-SFB) is formed (right).

in vivo biodistribution of the AuNPs, we employed positron emission tomography (PET). PET is a highly sensitive, noninvasive isotopic imaging tool that allows the determination of quantitative pharmacokinetics by imaging the uptake of the candidate nanoparticles (NPs). In addition to conventional *ex vivo* biodistribution techniques, PET studies can also provide a reliable biodistribution profile for nanomaterials.[9] One drawback of the traditional use of radiometal-chelator complexes for biodistribution studies is that the radiometal can detach from the surface of the NPs either by a leaching process or through *in vivo* displacement from complexes as a result of transchelation in the presence of high plasma protein concentrations. As a result, the *in vivo* data may fail to reflect the true pharmacokinetics and biodistribution of the NPs.[10,11] However, there are stable complexes of ^{64}Cu[12] and ^{68}Ga[13] that can be used for *in vivo* applications. In this work we covalently bound the label *N*-succinimidyl-4-[^{18}F]-fluorobenzoate ([^{18}F]-SFB) to the C(AuNP)LPFFD conjugate. ^{18}F has been used to label a variety of nanoparticles, including magnetic-upconversion nanophosphors,[14] quantum dots,[15] and lipid-shelled microbubbles,[16] and recently in our group diamond nanoparticles were labeled with [^{18}F]-SFB.[17] To the best of our knowledge, this study represents the first time that AuNPs have been labeled with the radioisotope ^{18}F for PET imaging.

We used the probe [^{18}F]-SFB, which reacts with primary and secondary amino groups[17,18] to label the conjugate. In the C(AuNP)LPFFD conjugate, the α-amino group of the Cys residue (C) is hidden because of its adsorption onto the gold surface[19,20] and is thus unavailable for interaction with the probe. The C residue contains a thiol group that is chemisorbed easily to the gold surface. To provide an available amino group for the reaction with [^{18}F]-SFB and to take advantage of the possibility of NPs multifunctionalization, the AuNPs were functionalized with two peptides, CLPFFD and CK, to obtain the conjugate C(AuNP)LPFFD−C(AuNP)K (Figure 1). The introduction of the dipeptide CK into the NP provided an additional amino functionality through the K side chain, which can react with the radioactive [^{18}F]-SFB moiety. After the synthesis of the probe, the biodistribution of the radiolabeled conjugate C(AuNP)LPFFD-C(AuNP)K([^{18}F]-SFB) (Figure 1) was studied by PET.

■ EXPERIMENTAL PROCEDURES

Synthesis of Peptides CK and CLPFFD. The peptides were synthesized manually on H-Rink Amide ChemMatrix resin (100 mg, 0.68 mmol/g) and chlorotrityl resin (100 mg, 1 mmol/g) using a Fmoc/tBu strategy for CLPFFD and CK, respectively, in polypropylene syringes, each fitted with a polyethylene porous disk. Solvents and soluble reagents were removed by suction. CLPFFD and CK are amide and carboxy C-terminal, respectively. Washings between deprotection, couplings, and subsequent deprotection steps were carried out with DMF and DCM using around 10 mL solvent per gram of resin each time. The Fmoc group was removed by treatment with a mixture of piperidine−DMF (1:4 v/v) (2 × 10 min). After Fmoc removal, coupling reactions were carried out with Fmoc-amino acids (4 equiv), HOAt (4 equiv), and DIC (4 equiv) in DMF for 1.5 h. The Kaiser colorimetric test assay[21] was used for the detection of solid-phase primary amines, while the De Clercq[22] test was used for secondary amines bound to solid phase.

When necessary, recouplings were done with PyBOP (4 equiv), HOAt (4 equiv), and DIEA (12 equiv) for 1.5 h. For the deprotection of side chain groups and concomitant cleavage of the peptides from the support, the resin was washed with DCM (3 × 1 min), dried, and treated with a TFA-H_2O-TIS (95:2.5:2.5) cocktail for 1 h. TFA was then removed by evaporation with a N_2 stream and peptides were precipitated with cold anhydrous *tert*-butyl methyl ether (TBME), dissolved in H_2O-MeCN (1:1) and freeze−dried. The crude peptides were purified using a semipreparative RP-HPLC [Waters 2487 Dual λ Absorbance Detector (Waters, MA, USA) equipped with a Waters 2700 Sample Manager, a Waters 600 controller, a Waters Fraction Collector, a Symmetry column (C18, 5 μm, 30 × 100 mm), and Millenium software with a flow rate of 10 mL/min in a gradient of 0−20% B for 5 min, 20−40% B for 35 min, 40−100% B]. Peptides were desalted using a NAP10 Sephadex G25 column. The column was equilibrated with 10 mL of H_2O and the peptide was then loaded (10 mg/mL) and eluted with H_2O. One mL fractions were collected and analyzed by RP-HPLC. Fractions containing the peptide were lyophilized.

Peptides were characterized by MALDI-TOF mass spectrometry [Voyager-DE RP MALDI-TOF, PE Biosystems with a N_2 laser of 337 nm], by HPLC-MS [Waters Alliance 2695 equipped with 2998 photodiode array detector, ESI-MS micromass ZQ, Sunfire C18 column (2.1 mm × 100 mm, 3.5 μm, Waters) and *Masslynx* software; flow rate = 0.3 mL/minute; gradient = 0−100% B in 8 min (A = 0.1% formic acid in H_2O, and B = 0.07% formic acid in MeCN)], by high resolution mass spectra were recorded on a LTQ-FT Ultra (Thermo Scientific) and by analysis of amino acids [Waters 600 equipped with a Delta 600 pump, 2487 UV detector, 717 automatic injector, Waters AccQ-tag amino acids analysis column Nova-pak C18 (3.9 × 150 mm, 4 μm, Waters), and *Masslynx* software].

Synthesis of AuNPs. Citrate-coated AuNPs (12 ± 0.5 nm) were prepared by citrate reduction of $HAuCl_4$. An aqueous solution of $HAuCl_4$ (100 mL, 1 mM) was refluxed for 5−10 min, and a warm (50−60 °C) aqueous solution of sodium citrate (10 mL, 38.8 mM) was added quickly. Reflux was continued for another 30 min until a deep red solution appeared. The solution was filtered through a 0.45 μm Millipore syringe filter to remove any precipitate, pH was adjusted to 7.4 by adding dilute NaOH solution, and the final colloid solution was stored at 4 °C. AuNP were observed by transmission electronic microscopy (TEM) using a JEOL JEM-1010 microscope. The specimen was prepared by dropping AuNPs on Formvar carbon-coated copper microgrids and letting them dry. UV−vis absorption spectra were recorded at room temperature with a Unicam UV−vis spectrophotometer (UV3).

Obtention of C(AuNP)LPFFD-C(AuNP)K. The AuNP−peptide conjugates were prepared by mixing a colloidal gold solution with peptide solutions containing CLPFFD and CK in various proportions to obtain functionalized gold surfaces. 1 mL aliquots of the peptide solutions were added to 20 ml of AuNPs Solutions to reach the different proportions of CK/CLPFFD: 4 mM/1 mM, 2 mM/1 mM, 1 mM/1 mM, and 1 mM/2 mM. The most stable C(AuNP)LPFFD-C(AuNP)K conjugates were obtained by mixing a 5.2 nM AuNP solution with a mixture of CK/CLPFFD (4 mM/1 mM). The conjugation was performed in the presence of excess peptide to ensure full conversion of the AuNPs.

The conjugates were purified first through a 450 nm filter and then by 3 days of dialysis in a Spectra/Por MWCO 6−8000 membrane against 1.2 mM sodium citrate (6 buffer changes) to eliminate excess peptide. UV−vis absorption spectra were recorded at room temperature with a Unicam UV−vis spectrophotometer (UV3). To confirm the absence of nonconjugated peptide, 3 mL of the conjugated solution was centrifuged at 13500 rpm for 30 min to provide AuNP−peptide sediments. The supernatant was then evaporated to dryness, and an amino acid analysis was carried out.

Determination of AuNP Concentration and Estimation of the Number of Peptide Molecules Per Nanoparticle. The peptide load of the AuNPs was calculated by dividing the amount of peptide grafted [obtained by amino acid analysis (AAA) of the pellet] by the amount of AuNPs in solution, estimated according to Liu et al.[23] by considering the number of gold atoms per nanoparticle according to the size determined by TEM and the concentration of gold in the solution obtained by inductively coupled plasma mass spectrometry (ICP-MS).

The ICP-MS determinations were carried out in triplicate. The ICP multielement standard was obtained from high purity standards (QCS-26). The samples were digested in a Milestone MLS-1200 Mega plus EM-45 microwave oven using USEPA Method IO-3.1. To summarize, this method consisted of the extraction of the elements using a nitric acid−hydrogen peroxide (10:1) solution. After the digestion process, the gold concentration was directly determined by ICP-MS (Agilent, ICP-MS 7500 cx with collision chamber).

The average number of gold atoms per nanoparticle could be calculated from the TEM analysis. Using the *ImageJ* software, the average core diameters of the particles (D, nm) were measured. Assuming a spherical shape and a uniform fcc structure, the average number of gold atoms (N) for each type of nanosphere was calculated by eq 1, where ρ is the density for fcc gold (19.3 g/cm^3) and M represents the atomic weight of gold (197 g/mol):

$$N = \pi \rho D^3/6M = 30.89602\ D^2 \qquad (1)$$

The concentration of AuNPs solution was 5.2 ± 0.2 nM.

To determine the peptide concentration, an amino acid analysis was performed on the pellet obtained following the centrifugation of the conjugates at 13500 rpm (16200 × *g*) for 30 min, conditions that result in the sedimentation of the NPs. The number of peptide molecules per AuNP was obtained by dividing the number of peptide molecules per milliliter of solution by the number of particles per milliliter of solution. This ratio was obtained in triplicate in three independent repetitions of the synthesis and conjugation procedure. There were 122 ± 5 and 75 ± 5 molecules of CK and CLPFFD per nanoparticle, respectively.

Preparation of [^{18}F]-SFB. The synthesis was performed in assembled Eckert & Ziegler modules following the methodology described by Mäding et al.[24] with minor changes. Briefly, [^{18}F] was produced by the bombardment of [^{18}O]-H_2O with high-energy protons (18 MeV) in an 18/9 IBA cyclotron. The radioisotope [^{18}F] was sent to the automatic module where it was contained in a QMA cartridge. Then, [^{18}F] was extracted into the reactor by passing a mixture of 2 mg of K_2CO_3 and 1.8 mg of Kryptofix 222 in 0.8 mL of a 1:1 mixture of H_2O/CH_3CN through the QMA cartridge. The reactor was heated at 100 °C, and He flow and vacuum were applied for 5 min to dry the [^{18}F]. To ensure that the drying process went to completion, an extra 1 mL of anhydrous CH_3CN was added to dry the mixture, as described above, with an extra 5 min of vacuum applied.

Next, a solution of 5 mg of 4-(*tert*-butoxycarbonylmethyl)-phenyl trimethylammonium trifluoromethanesulfonate in 1 mL of anhydrous CH_3CN was added to the dried [^{18}F]. The mixture was stirred for 10 min at 90 °C, and 0.5 mL of 1 M HCl was then added to the solution. The reaction mixture was heated at 100 °C for 5 min. After cooling to 25 °C, the reaction mixture was diluted with 9 mL of water and passed through a C18 HELA cartridge for solid extraction. Subsequently, 3 mL of CH_3CN was passed through the cartridge, and the solution was sent to a second reactor. This eluate was treated with 20 mL of 25% methanolic Me_4NOH in 500 mL of CH_3CN. The reaction mixture was then dried at 90 °C by passing a continuous He flow and applying vacuum. The drying process was completed by the addition of another 3 mL of anhydrous CH_3CN. Then, a solution of 15 mg of *N,N,N′,N′*-tetramethyl-*O*-(*N*-succinimidyl)uronium tetrafluoroborate in 500 mL of anhydrous CH_3CN was added, and the mixture was heated at 90 °C for 2 min. The mixture was cooled to 25 °C and diluted with 5% aqueous acetic acid. The crude product was purified with semipreparative HPLC using a Teknokroma Mediterranean Sea-18 (25 cm × 1 cm, 5 mm) column in isocratic mode with a mobile phase composed of a 42.5:57.5 ratio of CH_3CN/ammonium formiate (3.15 g/1 L H_2O, pH = 5) at 5 mL/min. The purification was monitored by isotopic and UV−vis (254 nm) detectors. The desired fraction (9−11 min) was collected in 20 mL of 0.9% saline solution. This solution was passed through a C18 cartridge, rinsed with 20 mL of water, and extracted with 3 mL of anhydrous acetone. One aliquot was submitted for quality control, and the remaining solution was dried with gaseous N_2. The quality control was performed by HPLC using a Teknokroma Mediterranean Sea-18 (25 mm × 0.46 cm, 5 mm) column in gradient mode with a flow rate of 2 mL/min and CH_3CN/ammonium formate (3.15 g/1 L H_2O, pH = 5) as a mobile phase, starting at a 10:90 ratio and reaching 40:60 in 10 min. The eluent was monitored by isotopic and UV−vis (254 nm) detectors. The desired compound, [^{18}F]-SFB, eluted at 10.3 min. Under these reaction conditions, we achieved a 37% yield (decay corrected) of [^{18}F]-SFB that had purity >99% and 110 ± 15 GBq/μmol of specific activity.

Preparation of C(AuNP)LPFFD-C(AuNP)K([^{18}F]-SFB). Two mL of a 5.2 nM solution of C(AuNP)LPFFD-C(AuNP)K was centrifuged at 4200 rpm (1980 × *g*) for 15 min. The supernatant was then removed, and a mixture containing 20 μL of DMSO and 80 μL of 1.2 mM of sodium citrate (pH = 10) was added to the solid. The resulting red solution was added to 4.44 ± 1.11 GBq of the solid residue of [^{18}F]-SFB. The mixture was stirred at 50 °C for 1 h. After this incubation, 900 μL of 1.2 mM of sodium citrate solution (pH = 10) was added to the red mixture and centrifuged at 4200 rpm (1980 × *g*) for 15 min. The solid was washed 3 times, and the radioactivity of the liquid was monitored each time with an activimeter. Following the final wash, the washing solution contained no radioactivity. Finally, the solid was dissolved in a mixture of 2 mL of 1.2 mM of sodium citrate (pH = 10) and 50 μL of Tween-80, maintaining the characteristic red color. The labeling yield of AuNPs was 0.8 ± 0.3%. There were 27 ^{18}F atoms per nanoparticle. The radiolabeling yield was decay-corrected and calculated from the initial pure [^{18}F]-SFB content added to the reaction.

Zeta Potential. The zeta potential (ZetaSizer 3000, Malvern Instruments, UK) measurements of the nanoparticles were performed five times in solution. Because the zeta potential measurements were performed in an aqueous solution, the Smoluchowski approximation was used to calculate the zeta potential from the measured electrophoretic mobility. The measurements were conducted with a disposable polycarbonate capillary cell (DTS 1061, Malvern) under precise temperature control (25 °C). The concentration of C(AuNP)-LPFFD-C(AuNP)K(SFB) was 5.2 nM, the solution of the nanoparticles was 1.2 mM citrate (pH = 7.4). The concentration of C(AuNP)LPFFD-C(AuNP)K was 5.2 nM, and the solution was citrate at pH = 7.4 .

Dynamic Light Scattering (DLS). A Malvern ZetaSizer Nano ZS instrument (Malvern Instruments, UK) operating at a wavelength of 633 nm and a fixed scattering angle of 173° was used to measure the NP sizes. An aliquot of 1 mL of each solution was placed in a cell for the DLS analyses. The measurements were conducted with a disposable polycarbonate capillary cell (DTS 1061, Malvern) under precise temperature control (25 °C). The concentration of C(AuNP)LPFFD-C(AuNP)K was 5.2 nM, and the media was sodium citrate (pH = 7.4). The concentration of C(AuNP)LPFFD-C(AuNP)K-(SFB) was 5.2 nM the media was sodium citrate (pH = 7.4). In addition we carried out DLS measurements of both conjugates at different concentrations using citrate 1.2 mM pH 7.4 and PBS as dissolvent, respectively.

Stability of the Conjugate in PBS. A 500 μL aliquot of the conjugate solution (5.2 nM) was mixed with 500 μL of PBS, and the resulting mixture was incubated at room temperature (25 °C) and at 37 °C for 7 days. UV−vis absorption spectra were recorded at room temperature with a Unicam UV−vis spectrophotometer (UV3).

Stability of C(AuNP)LPFFD-C(AuNP)K(SBF) in Plasma. To determine the plasma stability of the conjugate, 1 mL aliquots of the conjugate (5.2 nM) were centrifuged at 13200 rpm (16200 × *g*) for 15 min, and the resulting pellets were resuspended in plasma and incubated at 37 °C. The samples were centrifuged at 13200 rpm (16200 × *g*) and resuspended in citrate pH = 7.4. The UV−visible spectra, DLS analyses, and zeta potential measurements were obtained after 1, 2, 4, and 24 h.

Stability of C(AuNP)LPFFD-C(AuNP)K([^{18}F]-SBF) in Plasma. The pellet obtained after preparing and washing (3×) the labeled conjugate C(AuNP)LPFFD-C(AuNP)K-([^{18}F]-SBF) (10 ± 4 μCi) was resuspended in 1 mL of plasma and incubated at 37 °C. Aliquots of 150 μL were removed at different time periods up to three hours and centrifuged at 16200 × *g* during 10 min. The radioactivity was determined in the supernatants and pellets. The proportion of radioactivity in the supernatants was determined by dividing the radioactivity in the supernatant by the total radioactivity of the sample (supernatant + pellet).

Animals. Adult male Sprague−Dawley rats weighing 571 ± 112 g (mean ± standard deviation; Charles River, Spain; $n = 3$) were used in this study. The animal studies were conducted in compliance with the Spanish legislation on the Protection of Animals Used for Experimental and Other Scientific Purposes and in accordance with the Directives of the European Union.

PET Image Acquisition. The animals were anesthetized with isoflurane vaporized in O_2 and received an intravenous bolus injection of 3.1 ± 2.7 kBq (mean ± standard deviation) of ^{18}F-radiolabeled nanoparticles. Immediately after injection, the animals were placed in an animal-dedicated camera (microPET R4; Concorde, Siemens, Knoxville, TN, USA) for dynamic whole body image acquisition. Whole body data were acquired for 120 min. During all of the acquisition procedures, the anesthesia was maintained with a facial mask and a concentration of 2.5% of isoflurane vaporized in O_2.

Image Analysis. To obtain dynamic whole body images (frames = 18), the PET data were corrected for detector nonuniformity, random coincidences, and radionuclide decay, but not for photon scatter or attenuation. The images were then reconstructed into a matrix size of 128 × 128 × 63 and a voxel size of 0.85 × 0.85 × 1.21 mm^3 with a filtered backprojection algorithm (FBP). After reconstruction, volumes of interest (VOI) were manually drawn in the different organs, and the time−activity curves were calculated. One of the VOIs was placed in the heart region to obtain a representative measurement of the concentration of radioactivity in blood. The concentration of radioactivity obtained at the end of the acquisition was used to calculate the percentage of the injected dose for each gram of tissue based on the PET data. Mean activity curves for the three animals were also calculated for each organ.

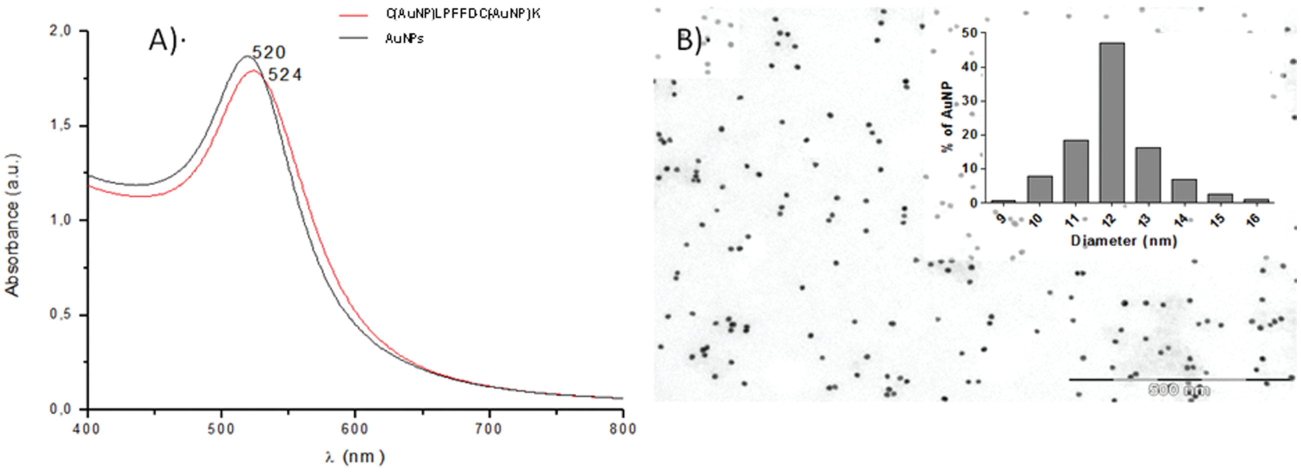

Figure 2. (A) UV−vis spectra of AuNPs and C(AuNP)LPFFD-C(AuNP)K . (B) TEM micrograph of C(AuNP)LPFFD-C(AuNP)K. The inset shows the size distribution. The bar represents 500 nm.

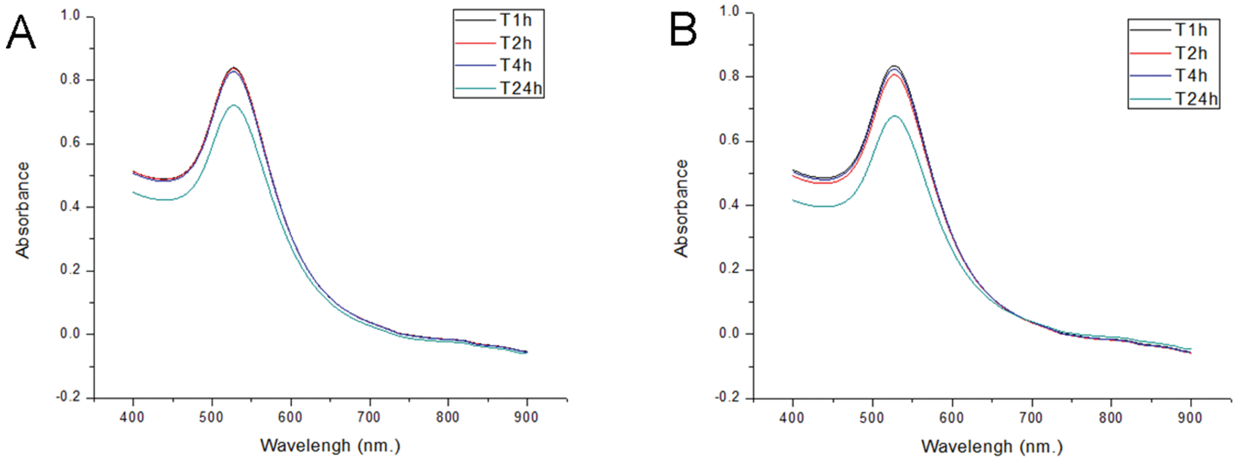

Figure 3. UV−vis spectra of the conjugate C(AuNP)LPFFD-C(AuNP)K(SFB) in PBS after incubation for different periods of time at 25 °C (A) and at 37 °C (B).

■ RESULTS AND DISCUSSION

Synthesis and Characterization of C(AuNP)LPFFD-C(AuNP)K(SFB). AuNPs with a diameter of 12 nm were obtained using the sodium citrate reduction method.[25] The AuNP−peptide conjugates were prepared by mixing the AuNPs solution with a solution of CK and CLPFFD. The most stable C(AuNP)LPFFD-C(AuNP)K conjugate was obtained by mixing a 5.2 nM AuNPs solution with a mixture of CK/CLPFFD (4 mM/1 mM). We performed the conjugation using different proportions of the peptides (see Experimental Procedures section) and studied the stability of the resulting conjugates by determining the UV−vis spectra, DLS, and zeta potential properties over time. In the case of the conjugates prepared from the 4 mM/1 mM solution, the plasmon band remained centered at the same position with respect to time, as did the hydrodynamic diameters (Supporting Information Figure S3). In contrast, a shift to higher wavelengths or a band broadening was observed in the UV−vis spectra of the conjugates prepared by using different CK/CLPFFD ratios (for 2/1; 1/2), and an increase in the hydrodynamic diameter was observed for all of the conjugates (2/1, 1/2, 1/1). On the other hand, the zeta potential values observed for the conjugate prepared from 4 mM/1 mM solution not significant variations were appreciated.

The peptides were synthesized by solid phase synthesis following a Fmoc/tBu protocol and were characterized by HPLC and mass spectrometry (Supporting Information, Figures S1, S2 and Table S1). The conjugates were exhaustively characterized by various techniques [UV−vis, transmission electron microscopy (TEM), X-ray photoelectron spectroscopy (XPS), dynamic light scattering (DLS), and zeta potential; see Supporting Information]. The UV−vis spectra showed a defined plasmon resonance peak at 520 nm (Figure 2), which was attributed to the presence of AuNPs with a diameter of approximately 12 nm. After conjugation with CK and CLPFFD, the wavelength of maximum absorption shifted to longer wavelengths with respect to AuNPs (524 and 520 nm, respectively) as a result of the capping of the AuNP surfaces with the peptide molecules. The TEM images showed particles (12 ± 0.5 nm) with regular shapes and a narrow size distribution (Figure 2).

Further characterization of C(AuNP)LPFFD-C(AuNP)K by XPS was performed. The peaks expected from the S 2p, S 2s, and Au 4f core levels were detected. High-resolution data were also recorded in the S 2p, S 2s, and Au 4f spectral regions. The S 2p signal consisted of a broad band with a maximum at 162.2 eV that corresponds to the chemisorption of sulfur grafted onto gold (Supporting Information, Figure S4).

The peptide load of AuNP was calculated by dividing the amount of peptide grafted [obtained by the amino acid analysis (AAA) of the pellet] by the amount of AuNPs in solution determined by ICP-MS and considering the diameters obtained by TEM according with Liu et al.[23] For each nanoparticle, there were 122 and 75 molecules of CK and CLPFFD present, respectively.

To incorporate *N*-succinimidyl-4-fluorobenzoate (SFB) into the conjugates, the NPs were centrifuged and resuspended in a 1:4 DMSO:1.2 mM sodium citrate mixture (pH = 10) that had been mixed with SFB to render the conjugate C(AuNP)-LPFFD-C(AuNP)K(SFB) by a reaction between SFB and the primary ε-amino group of the lysine residue of the CK peptide anchored to the AuNPs (Figure 1). According to the DLS and zeta potential measurements, the NPs had a hydrodynamic diameter of 23 nm (PI:0.3) and −43± mV, respectively. DLS measurements were carried out by using a 633 nm laser which could complicate the dynamic light scattering measurements due to the absorbance of the particles.[26] In order to discard effects given by the concentration of the samples, we carried out the measurements at different concentrations of nanoparticles, and no appreciable changes in the intensities and sizes of the nanoparticles were observed (Supporting Information, Figure S5).

Prior to any *in vivo* examination of C(AuNP)LPFFD-C(AuNP)K(SFB), *in vitro* stability studies were carried out in PBS at 25 and 37 °C (Figure 3). The conjugate was incubated with PBS, and UV−vis spectra were obtained. In Figure 3, one can see that the plasmon peak remains unchanged, allowing us to conclude that the colloids were stable at the two tested temperatures in PBS.

We also studied the stability of these nanoparticles in plasma, a condition that more faithfully reproduces the *in vivo* environment. By UV−vis, we observed a shift in the plasmon band from 527 nm (for the conjugate before incubation with plasma as can be seen in Figure 3) to 531 nm, which could be attributed to the capping of the nanoparticles with proteins to form the protein corona (Supporting Information, Figure S6), in accord with Olmedo et al.[19] In addition, we carried out DLS experiments in which we observed the presence of different populations of different sizes. In samples incubated for 1 h, two different populations of particles were observed where one is centered at 45 nm and the other at 500 nm, which could be attributed to a capping with proteins and/or to aggregation process. After 2 h, there was an increase in the sizes of the nanoparticles which could be attributed to aggregation processes. On the other hand, we carried out zeta potential measurements observing that there were no dramatic variations on the corresponding values with the incubation time (Supporting Information, Figure S6).

For the biodistribution studies, the C(AuNP)LPFFD-C(AuNP)K(SFB) conjugate was capped with Tween-80 to increase its stability under physiological conditions. After the injection of the nanoparticles into the plasma, the aforementioned capping occurs, and dilution could cause the desorption of Tween and consequent aggregation. To test the conjugate under conditions resembling this physiological scenario, we used UV−vis to study the stability of the conjugate capped with Tween and incubated with plasma after dialysis against PBS for 48 h (Supporting Information Figure S7). The UV−vis spectra of the conjugates were taken at different times, and it was observed that no modifications of the spectra occurred within the first 24 h. A small diminution of the intensity band was observed at 48 h without an observable broadening. From these results, we can infer that the depletion of the Tween detergent by the filtration and the dilution during dialysis did not induce a significant aggregation.

The labeled conjugate was obtained by reaction with [^{18}F]-SFB. This reaction had a labeling efficiency of about 1% as determined by radioactivity counting. The labeled NPs in PBS solution were stable for at least 5 h (according to UV−vis spectra, data not shown).

To probe the stability of the labeled conjugate C(AuNP)-LPFFD-C(AuNP)K([^{18}F]-SFB), we carried out stability studies at 37 °C. We incubated the C(AuNP)LPFFD-C(AuNP)K-([^{18}F]-SFB) conjugate in plasma at 37 °C, and samples from the incubation mixture were taken at different times for 3 h and were then centrifuged. The centrifugation procedure used was sufficient to separate the [^{18}F]-AuNPs from the radioactive degradation products. Therefore, the amount of radioactivity in the supernatant is proportional to the degree of degradation of the radiolabeled nanoparticles. The supernatants and pellets were counted in a well counter, and the percentage of radioactivity in the supernatant is shown in Supporting Information (Figure S8). Radioactivity was observed in both fractions supernatant and pellet. The presence of radioactivity in the supernatants could be attributed to free metabolites or to the presence of [^{18}F]-AuNPs nanoparticles that did not sediment after centrifugation. As was mentioned previously, nanoparticles in plasma are in a different aggregation state. Notably, it is necessary to consider for *in vivo* experiments that from the beginning of the incubation there is a free labeled species that could be filtered by the kidney and consequently excreted by a renal mechanism. Remarkably, it is important to mention that the radioactivity content in plasma was constant with time, which was not compatible with the detachment of the radiolabel from the AuNPs after incubation. Rather, a time-dependent increase in the radioactivity of the supernatant would be expected as a consequence of the detachment of the radiolabel, which does not occur in this case.

In Vivo Distribution of C(AuNP)LPFFD-C(AuNP)K([^{18}F]-SFB). The biodistribution of the newly synthesized conjugate was monitored by PET imaging at various time points following intravenous injection into rats. Figure 4 shows PET images of

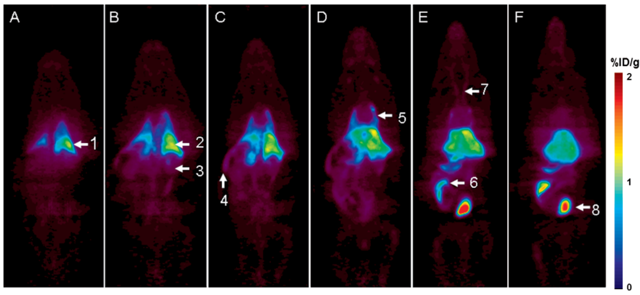

Figure 4. Representative image of a 120 min PET scan after an intravenously injection of a 5.2 nM solution of C(AuNP)LPFFD−C(AuNP)K([^{18}F]-SBF) in rats. Coronal sections of the animal from dorsal (A) to ventral (F). Organs that presented elevated uptake of the radiolabeled compound are clearly seen. Liver appears in all the images, arrows 1 and 2. Lungs can be visualized in images A−E (5). Kidneys and spleen can be visualized in images B and C, arrows 3 and 4. Bladder and intestines are clearly visible in images E and F, arrows 8 and 6. Interestingly, supraortic vessels can be appreciated in image E, arrow 7.

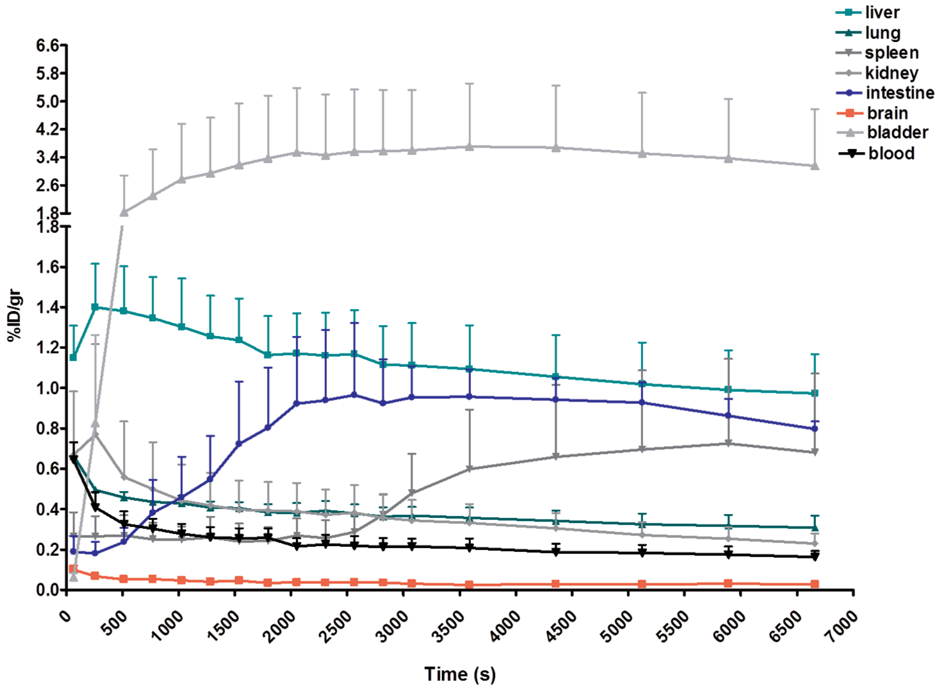

Figure 5. Mean time−activity curves of the levels of radioactivity in the different organs obtained from the PET images. The bars represent the standard deviation. The radioactivity accumulated in the bladder and intestine, reflecting the dual excretory mechanisms of the nanoparticle.

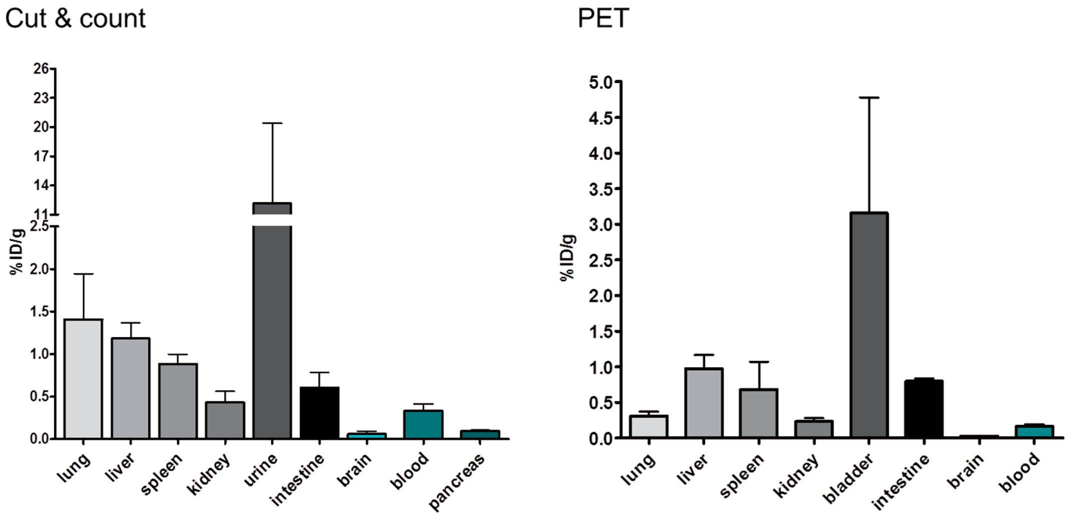

Figure 6. Graphs showing the %ID/gr in each tissue calculated from the cut and count study or the PET scans.

the labeled AuNPs, demonstrating that elevated concentrations of radioactivity could be observed in the kidneys, liver, bladder, and intestine 120 min after injection. The spleen was clearly visible in the images of all the animals, indicating considerable trapping of the NPs by the reticuloendothelial system (RES), a finding that is consistent with our previous *ex vivo* results in rats.[8] Moreover, the lungs showed high levels of radioactivity, thereby suggesting the trapping of the conjugate in the vascular bed of this organ which could be attributed to the presence of species of high size (approximately 500 nm). The great vessels were visible in the images, which could indicate the binding of the labeled compound to the vascular endothelium. Alternatively, these images could represent the blood volume of the vessels produced by the nanoparticles that remained in the blood until the end of the experiment. The supraortic vessels were visible in the images, indicating the binding of the labeled compound to the vascular endothelium. Other tissues, including the brain, displayed low levels of radioactivity, which could be related to the rapid washout of the conjugate from the blood (see Figure 4).

The time−activity curves obtained from the PET images showed that the highest concentration of the compound was present in the bladder, indicative of the urinary excretion of the NPs (Figure 5). The intestine also progressively accumulated radioactivity, which is compatible with the biliary excretion of the conjugate. A time−activity curve of radioactivity in the spleen showed that the accumulation of the conjugate was high at the beginning of the scan and increased only slightly with time, a pattern compatible with the phagocytosis of the circulating NPs by the RES components of this organ. The concentration of radioactivity in the blood decreased quickly during the first minutes of the study in parallel with an increase in the urine, reflecting the rapid urinary excretion of part of the injected dose. After this initial rapid decline, the radioactivity in blood decreased slowly, similar to the liver, lung, and kidney. Finally, the brain contained a very low level of radioactivity. This level decreased with time, which possibly reflects the clearance of the compound from the vascular compartment.

The results calculated from the PET images showed similar values of the percentage of injected dose for each gram of tissue (%ID/gr) as the cut and count study (Figure 6). The calculation of %ID/gr from the cut and count results revealed that the urine contained the highest concentration of the radiolabeled compound. The presence of radioactivity in urine could be attributed to the filtration and excretion of nanoparticles or radioactive metabolites produced by the exchange of radioactive peptide molecules attached to the surface by thiolated molecules (i.e., peptides or proteins) present in the blood. To determine whether the measured radioactivity corresponded to the conjugate or to ^{18}F-labeled metabolites, we injected two animals with the labeled nanoparticles and collected their urine 1 h after injection. The urine samples were centrifuged under the same conditions described previously for the plasma stability experiment with the labeled conjugate. The results showed that the level of radioactivity in the supernatant was less than 0.02% of the total radioactivity in the urine (Supporting Information, Table S2). The fact that the total radioactivity observed in urine remained in the pellet after centrifugation could indicate that the signal observed in the urinary system in the microPET study corresponded to C(AuNP)LPFFD-C(AuNP)K([^{18}F]-SBF). However, renal excretion of free metabolites cannot be excluded due to the possible presence of them in the *in vivo* conditions, as was observed in the *in vitro* stability assay in plasma.

The lungs, liver, and spleen were the organs with the next highest levels of radioactivity, followed by the intestine, kidneys, and blood. The pancreas and brain, however, accumulated very low concentrations of radiolabeled nanoparticles. The results are in agreement with the %ID/gr observed in Figure 5. Only the results obtained from the bladder were clearly different from the results obtained in the urine count. However, this difference is only in the absolute magnitude of %ID/gr, not in its relationship with the values from the other tissues. In fact, the bladder also had the highest concentration of radioactivity in the PET quantification. The other tissues showed a similar pattern of radioactivity concentration and %ID/gr values as in the cut and count study. The differences observed in lung and blood was not significant and could be related to the low number of animals included in the study and the accuracy in the VOI delineation. We performed a statistical analysis of the data comparing the cut and count and PET results for the lung using Student's *t* test and the nonparametric Mann−Whitney test. In fact, because of the low resolution of the microPET systems, the signal from the liver could slightly increase the signal detected in the lung. This phenomenon is known as the partial volume effect. The influence of the partial volume effect on the results could potentially be reduced with a more precise delineation of the VOIs in the lungs, or by using a respiratory gating, or by avoiding the quantification of the inferior segments of these organs that are in the proximity of the liver. At the level of the heart, a VOI was delineated as a measurement of circulating blood, but this VOI also included the myocardium, contributing to the reduction in the %ID/gr observed in the PET study with respect to the cut and count study.

In summary, the conjugate C(AuNP)LPFFD-C(AuNP)K was covalently labeled with the probe [^{18}F]-SFB, producing a stable conjugate that allowed us to perform AuNPs biodistribution studies with PET imaging. The highest concentration of the radiolabeled conjugate was found in the bladder and urine and in a lower proportion in intestine, which showed progressive accumulation that was compatible with the biliary excretion of the conjugate. The AuNPs were removed by renal clearance; however, this process is efficient for NPs with a diameter below 5.5 nm. Under this size, NPs such as quantum dots can easily enter the urine by glomerular filtration or tubular secretion.[27] However, the renal clearance of larger NPs, including diamond nanoparticles and carbon nanotubes (CNTs), is also possible.[13,28] In addition to its metabolic function, the liver is also a major excretion route for larger NPs.[29,30] The excretion occurs across hepatocytes through the biliary production pathway. Hepatocytes have been shown to have phagocytic ability, although they are not as effective as Kupffer cells in capturing nanoparticles. Furumoto et al.[31] have found that polystyrene nanoparticles are taken up by both Kupffer cells and hepatocytes after intravenous administration.

The conjugate accumulated in liver and spleen, as was observed *ex vivo* in rats by our group[8] and by other authors for AuNPs of similar sizes.[32−36] This behavior can be attributed to the conjugate's negative superficial charge, which favors the interaction with the RES. When the NPs are administered, a variety of plasma proteins bind to their surfaces. The conjugates can then be recognized by the macrophage cell surface and internalized, leading to a significant loss of NPs from circulation. Some of the serum proteins that bind and cap the NPs are opsonins. These proteins may be recognized and captured by macrophages, thereby contributing to a major loss of the administered dose as a result of retention by the RES and the consequent accumulation in the liver and spleen.[8]

PET imaging allowed us to study the *in vivo* biodistribution of the AuNPs in a noninvasive and sensitive way using a reduced number of animals. Our results show that AuNPs can be covalently and radioactively labeled for PET biodistribution studies.

■ ASSOCIATED CONTENT

Ⓢ Supporting Information

Peptides HPLC and mass spectrometry, global yield of synthesis, X-ray photoelectron spectroscopy, obtention of conjugates with different proportions of peptides, stability of conjugates in plasma, radioactivity in urine. This material is available free of charge via the Internet at http://pubs.acs.org.

■ AUTHOR INFORMATION

Corresponding Author

*E-mail: mkogan@ciq.uchile.cl; albericio@irbbarcelona.org.

Author Contributions

□These authors contributed equally to the work.

Notes

The authors declare no competing financial interest.

■ ACKNOWLEDGMENTS

The authors would like to acknowledge Elisenda Coll of Serveis Cientificotècnics (Universitat de Barcelona) for assistance in transmission electronic microscopy. This work was supported by AECID, FONDECYT 1090143, MECESUP-UCH-0811, ACT-95, CICYT (CTQ2009-07758), the Instituto de Salud Carlos III (CB06_01_0074), the Generalitat de Catalunya (2009SGR 1024), the Institute for Research in Biomedicine, and the Barcelona Science Park, the CDTI under the CENIT Programme (AMIT Project) and the Spanish Ministry of Science and Innovation.

■ REFERENCES

(1) Bhattacharya, R., Mukherjee, P., Xiong, Z., Atala, A., Soker, S., and Mukhopadhyay, D. (2004) Gold Nanoparticles Inhibit VEGF165-Induced Proliferation of HUVEC Cells. *Nano Lett. 4*, 2479−2481.

(2) Kogan, M. J., Olmedo, I., Hosta, L., Guerrero, A. R., Javier Cruz, L., and Albericio, F. (2007) Peptides and Metallic Nanoparticles for Biomedical Applications. *Nanomedicine 2* (3), 287−306.

(3) Hosta, L., Olmedo, I., Arbiol, J., Cruz, L. J., Kogan, M. J., and Albericio, F. (2010) Multifunctionalized Gold Nanoparticles with Peptides Targeted to Gastrin-Releasing Peptide Receptor of a Tumor Cell Line. *Bioconjugate Chem. 21* (6), 1070−1078.

(4) Hosta, L., Pla-Roca, M., Arbiol, J., Lopez-Iglesias, C., Samitier, J., Cruz, L. J., Kogan, M. J., and Albericio, F. (2009) Conjugation of Kahalalide F with Gold Nanoparticles to Enhance in Vitro Antitumoral Activity. *Bioconjugate Chem. 20* (1), 138−146.

(5) Zharov, V. P., Mercer, K. E., Galitovskaya, E. N., and Smeltzer, M. S. (2006) Photothermal Nanotherapeutics and Nanodiagnostics for Selective Killing of Bacteria Targeted with Gold Nanoparticles. *Biophys. J. 90*, 619−627.

(6) Kogan, M. J., Bastus, N. G., Amigo, R., Grillo-Bosch, D., Araya, E., Turiel, A., Labarta, A., Giralt, E., and Puntes, V. F. (2006) Nanoparticle-mediated local and remote manipulation of protein aggregation. *Nano Lett. 6* (1), 110−115.

(7) Araya, E., Olmedo, I., Bastus, N. G., Guerrero, S., Puntes, V. F., Giralt, E., and Kogan, M. J. (2008) Nanoparticles and Microwave Irradiation Inhibit Beta-Amyloid Amyloidogenesis. *Nanoscale Res. Lett. 3*, 435−443.

(8) Guerrero, S., Araya, E., Fiedler, J. L., Arias, J. I., Adura, C., Albericio, F., Giralt, E., Arias, J. L., Fernández, M. S., and Kogan, M. J. (2010) Improving the Brain Delivery of Gold Nanoparticles by Conjugation with an Amphipathic Peptide. *Nanomedicine 5*, 897−913.

(9) Reiner, T., Keliher, E. J., Earley, S., Marinelli, B., and Weissleder, R. (2011) Synthesis and In Vivo Imaging of a ^{18}F-Labeled PARP1 Inhibitor Using a Chemically Orthogonal Scavenger-Assisted High-Performance Method. *Angew. Chem., Int. Ed. 50*, 1922−1925.

(10) Xiea, H., Wang, Z. J., Bao, A., Goins, B., and Phillips, W. T. (2010) In Vivo PET Imaging and Biodistribution of Radiolabeled Gold Nanoshells in Rats with Tumor Xenografts. *Int. J. Pharm. 395*, 324−330.

(11) Zhou, M., Zhang, R., Huang, M., Lu, W., Song, S. H., Melancon, M. P, Tian, M., Liang, D., and Li, C. (2010) A Chelator-Free Multifunctional [^{64}Cu]CuS Nanoparticle Platform for Simultaneous Micro-PET/CT Imaging and Photothermal Ablation Therapy. *J. Am. Chem. Soc. 132* (34), 15351−15358.

(12) Yang, X. Q., Hong, H., Grailer, J. J., Rowland, I. J., Javadi, A., Hurley, S. A., Xiao, Y. L., Yang, Y. A., Zhang, Y., Nickles, R., Cai, W. B., Steeber, D. A., and Gong, S. Q. (2011) cRGD-functionalized, DOX-conjugated, and (64)Cu-labeled superparamagnetic iron oxide nanoparticles for targeted anticancer drug delivery and PET/MR imaging. *Biomaterials 32* (17), 4151−4160.

(13) Ambrosinia, V., Campana, D., Tomassetti, P., Grassetto, G., Rubello, D., and Fantia, S. (2011) PET/CT with (68)Gallium-DOTA-peptides in NET: An overview. *Eur. J. Radiol. 80* (2), E116−E119.

(14) Liu, Q., Sun, Y., Li, Ch., Zhou, J, Li, Ch., Yang, T., Zhang, X., Yi, T., Wu, D., and Li, F. (2011) ^{18}F-Labeled Magnetic-Upconversion Nanophosphors via Rare-Earth Cation-Assisted Ligand Assembly. *ACS Nano 5* (4), 3146−3157.

(15) Patt, M., Schildan, A., Habermann, B., Mishchenko, O., Patt, J. T., and Sabri, O. (2010) (18)F- and (11)C-labelling of quantum dots with n.c.a. [(18)F]fluoroethyltosylate and [(11)C] methyliodide: a feasibility study. *J. Radioanal. Nucl. Chem. 283* (2), 487−494.

(16) Tartis, M. S., Kruse, D. E., Zheng, H, Zhang, H, Kheirolomoom, A, Marik, J, and Ferrara, K. W. (2008) Dynamic microPET imaging of ultrasound contrast agents and lipid delivery. *J. Controlled Release 131* (3), 160−166.

(17) Rojas, S., Gispert, J. D., Martin, R., Abad, S., Menchón, C., Pareto, D., Víctor, V. M., Alvaro, M., Garcia, H., and Herance, J. R. (2011) Biodistribution of Amino-Functionalized Diamond Nanoparticles. In Vivo Studies Based on 18F Radionuclide Emission. *ACS Nano 5* (7), 5552−5559.

(18) Okarvi, S. M. (2001) Recent Progress In Fluorine-18 Labelled Peptide Radiopharmaceuticals. *Eur. J. Nucl. Med. 28*, 929−938.

(19) Olmedo, I., Araya, E., Sanz, F., Medina, E., Arbiol, J., Toledo, P., Alvarez-Lueje, A., Giralt, E., and Kogan, M. J. (2008) How Changes in the Sequence of the Peptide CLPFFD-NH$_2$ can Modify the Conjugation and Stability of Gold Nanoparticles and their Affinity for β-Amyloid Fibrils. *Bioconjugate Chem. 19*, 1154−1163.

(20) Guerrero, A. R., Caballero, L., Adeva, A., Melo, F., and Kogan, M. J. (2010) Exploring the Surface Charge on Peptide−Gold Nanoparticle Conjugates by Force Spectroscopy. *Langmuir 26* (14), 12026−12032.

(21) Kaiser, E., Colescott, R. L., Bossinger, C. D., and Cook, P. I. (1970) Color test for detection of free terminal amino groups in the solid-phase synthesis of peptides. *Anal. Biochem. 34* (2), 595−598.

(22) Madder, A., Farcy, N., Hosten, N. G. C., De Muynck, H., De Clercq, P. J., Barry, J., and Davis, A. P. A. (1999) Novel Sensitive Colorimetric Assay for Visual Detection of Solid-Phase Bound Amines. *Eur. J. Org. Chem. 11*, 2787−2791.

(23) Liu, X., Atwater, M., Wang, J., and Huo, Q. (2007) Extinction coefficient of gold nanoparticles with different sizes and different capping ligands. *Colloids Surf., B 58*, 3−7.

(24) Mading, P., Fuchtner, F., and Wuest, F. (2005) Module-assisted synthesis of the bifunctional labelling agent N-succinimidyl 4-[(18)F]fluorobenzoate. *Appl. Radiat. Isot. 66*, 329−332.

(25) Turkevich, J., Stevenson, P. C., and Hillier, J. (1951) A Study of the Nucleation and Growth Processes in the Synthesis of Colloidal Gold. *Discuss. Faraday Soc. 11*, 55−75.

(26) Hackley, A., and Clogston, J. D. (2011) Measuring the Hydrodynamic Size of Nanoparticles in Aqueous Media Using Batch-Mode Dynamic Light Scattering, Vol *697*, *Characterization of Nanoparticles Intended for Drug Delivery, Methods in Molecular Biology* (McNeil, S., Ed.) pp 32−52, Chapter 2, Human Press, UK.

(27) Choi, H. S., Liu, W., Misra, P., Tanaka, E., Zimmer, J. P., Ipe, B. I., Bawendi, M. G., and Frangioni, J. V. (2007) Renal Clearance Of Quantum Dots. *Nat. Biotechnol. 25*, 1165−1170.

(28) Lacerda, L., Soundararajan, A., Singh, R., Pastorin, G., Al-Jamal, K. T., Turton, J., Frederik, P., Herrero, M. A., Li, S., Bao, A., Emfietzoglou, D., Mather, S., Phillips, W. T., Prato, M., Bianco, A., Goins, B., and Kostarelos, K. (2008) Dynamic Imaging of Functionalized Multi-Walled Carbon Nanotube Systemic Circulation and Urinary Excretion. *Adv. Mater. 20* (2), 225−230.

(29) Yamago, S., Tokuyama, H., Nakamura, E., Kikuchi, K., Kananishi, S., Sueki, K., Nakahara, H., Enomoto, S., and Ambe, F. (1995) In vivo Biological Behavior of Water-Miscible Fullerenes. ^{14}C-Labeling, Absorption, Distribution, Excretion and Acute Toxicity. *Chem. Biol. 2*, 385−389.

(30) Cho, M. J., Cho, W. S., Choi, M., Kim, S. J., Han, B. S., Kim, S. H., Kim, H. O., Sheen, Y. Y., and Jeong, J. Y. (2009) The Impact of Size on Tissue Distribution and Elimination by Single Intravenous Injection of Silica Nanoparticles. *Toxicol. Lett. 189*, 177−183.

(31) Furumoto, K., Ogawara, K., Yoshida, M., Takakura, Y., Hashida, M., Higaki, K., and Kimura, T. (2001) Biliary Excretion of Polystyrene Microspheres Depends on the Type of Receptor-Mediated Uptake in Rat Liver. *Biochim. Biophys. Acta 1526*, 221−226.

(32) Lasagna-Reeves, C., Gonzalez-Romero, D., Barria, M., Olmedo, I., Clos, A., Ramanujam, V. M. S., Urayama, A., Vergara, L., Kogan, M. J., and Soto, C. (2010) *BBRC 393*, 649−655.

(33) Hillyer, J. F., and Albrecht, R. M. (2001) Gastrointestinal Persorption and Tissue Distribution of Differently Sized Colloidal Gold Nanoparticles. *J. Pharm. Sci. 90*, 1927−1936.

(34) Semmler-Behnke, M., Kreyling, W. G., Lipka, J., Fertsch, S., Wenk, A., Takenaka, S., Schmid, G., and Brandau, W. (2008) Biodistribution of 1.4- and 18-nm Gold Particles in Rats. *Small 4*, 2108−2111.

(35) De Jong, W. H., Hagens, W. I., Krystek, P., Burger, M. C., Sips, A. J., and Geertsma, R. E. (2008) Particle Size Dependent Organ Distribution of Gold Nanoparticles after Intravenous Administration. *Biomaterials 29*, 1912−1919.

(36) Sonavane, G., Tomoda, K., and Makino, K. (2008) Biodistribution of Colloidal Gold Nanoparticles after Intravenous Administration: Efect of Particle Size. *Colloids Surf., B 66*, 274−280.